Uncertainty budget for PTB's gonioreflectometers and ways to improve it in the short VIS spectral range

To cite this article: Irina Santourian *et al* 2022 *Metrologia* **59** 025004

View the article online for updates and enhancements.

Uncertainty budget for PTB's gonioreflectometers and ways to improve it in the short VIS spectral range

Irina Santourian[*], **Tatjana Quast and Alfred Schirmacher**

Physikalisch-Technische Bundesanstalt (PTB), Braunschweig, Germany

E-mail: irina.santourian@ptb.de

CrossMark

Abstract
This paper describes a detailed derivation of the uncertainty budget for measurements of the absolute spectral radiance factor with PTB's gonioreflectometers. The measurement uncertainty is determined according to the 'Guide to the expression of uncertainty in measurement' provided by the Bureau International des Poids et Mesures. To give an insight, the uncertainty analysis is applied to measurements of three ceramic samples. The influence of different systematic and statistical sources of uncertainty and their contributions are discussed in detail. For wavelengths larger than 450 nm the total measurement uncertainty is dominated by systematic contributions. Towards UVA the major contribution is caused by statistical effects, which are mainly due to the decreasing power of the radiation source used. We present an approach capable to reduce this contribution for the VIS/UVA-transition spectral range by means of a specially designed LED-based sphere radiation source.

Keywords: gonioreflectometer, measurement uncertainty analysis, absolute spectral radiance factor, BRDF, sphere radiation source, LED-sphere radiator

S Supplementary material for this article is available online

(Some figures may appear in colour only in the online journal)

1. The spectral radiance factor and its realization

1.1. Introduction

Diffuse reflection determined in directed geometries plays an important role in optical metrology applications and in many industrial sectors like automotive, paper, textile and color industry. It is a characteristic material property and its determination is required by numerous standards for quality control, e.g. [1–3] and related procedures for measurement underlie a continuous process of improvement, see e.g. scientific projects in [4] and related scientific committees cited therein. Calibrated reflection standards are also needed in research related activities, for example for space-based Earth observation and the material characterization of satellite components [5, 6].

The reference gonioreflectometer at the Physikalisch Technische Bundesanstalt (PTB) is the national standard for bidirectional diffuse reflectance measurements. It serves for the realization, preservation and dissemination of the scale of diffuse reflection in directed geometry and thus the determination of the absolute spectral radiance factor (SRF) $\beta(\lambda)$.

1.2. Description of PTB's gonioreflectometer facility

The reference gonioreflectometer at PTB, constructed in its original version by A Höpe [7] and modified since then in some detail, is a measurement facility dedicated to the determination of the absolute SRF $\beta(\lambda)$ in bidirectional geometries.
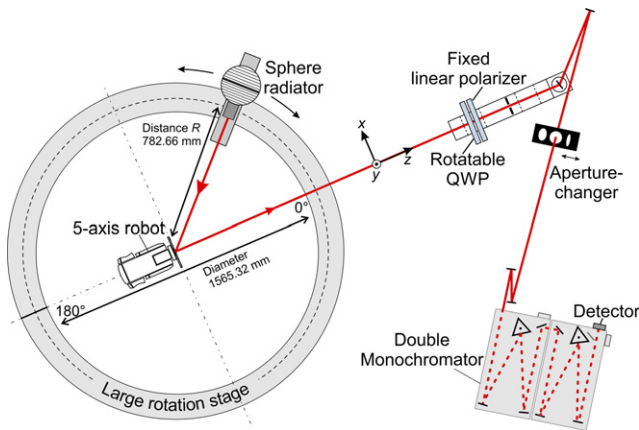
Figure 1. Schematic sketch of PTB's reference gonioreflectometer. Distance between the sample and the aperture changer is 3.8 m.

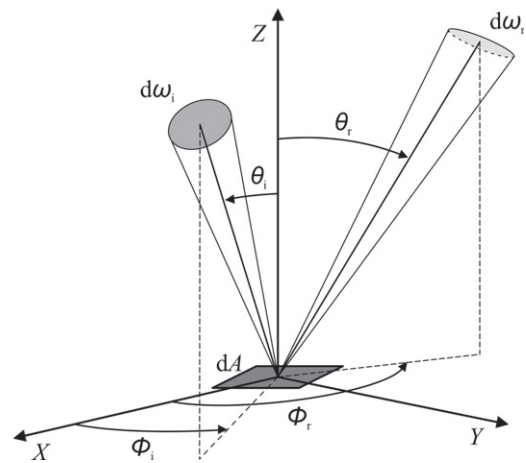**Figure 2.** Definition of directions and all associated angles.

The sample under test is placed on a five-axis robot arm in the center of the apparatus. For sample illumination a special integrating sphere radiation source is mounted on a large rotation stage and can be swivelled around the sample. The reflected radiation is collected by a fixed detection path consisting of the imaging optics, a double-monochromator and a detection system (electronics plus detector). On the detection side by default four different detector types can be used. A solar blind channel photomultiplier, a yellow enhanced channel photomultiplier, a silicon photodiode and a cooled InGaAs photodiode. All the signals are detected with a pico-amperemeter. In addition, in the very similar ARGon3 research goniometer a CCD camera can be used instead of a single element detector for simultaneous detection of the VIS spectral part [8]. For the data presented here measured in the range from 360 nm up to 850 nm a silicon photodiode was used.

A schematic sketch of the setup with the interaction of the described individual parts is shown in figure 1. This combination of robotic sample holder, mobile light source and fixed detection allows highly precise measurements of the SRF in almost any arbitrary bidirectional geometry, in-plane as well as out-of-plane, related to the plane spanned by the direction of illumination and the normal on the sample.

The radiation source plays a key role within the measuring process and concept. A homogenous radiation with high output and a highly Lambertian beam profile is required. Radiation is generated by a sphere radiator equipped with a 400 W quartz-tungsten halogen lamp [9]. This reliable halogen-sphere radiator (Halogen-SR) generates a spatially homogeneous, unpolarized irradiation and a high output in the VIS and NIR spectral range. Towards UVA the available output power decreases, which leads to a worse signal-to-noise ratio and thus to an increase in measurement uncertainty as will be shown in section 3. In an attempt to preserve the merit of the current radiator principle while enhancing the useable output, a radiator was developed which uses modern light-emitting diodes (LEDs) as radiation source. This LED-sphere radiator (LED-SR) in its present lay-out covers wavelengths from about 360 nm to 430 nm. It generates a much higher irradiance at short wavelengths compared with the halogen source and

considerably improves the signal quality and stability [10–12]. Both radiation sources have their advantages and can be used for the determination of the SRF as described below.

1.3. Spectral radiance factor and its measurement

The derivation of the general equation of the SRF $\beta(\lambda)$ is well described in several publications, e.g. in [2, 13]. Therefore, only a brief summary for further understanding is presented.

The SRF $\beta(\lambda)$ is defined as the ratio of the reflected spectral radiance $L_r(\lambda)$ of the sample and the reflected spectral radiance $L_r^{PRD}(\lambda)$ of the perfectly reflecting diffuser (PRD) irradiated under the same conditions

$$\beta(\lambda) = \frac{L_r(\lambda)}{L_r^{PRD}(\lambda)}. \qquad (1)$$

For the complete definition of the SRF as given below, the measurement geometry with all associated angles of incidence (index i) and reflection (index r) is required as shown in equation (2) and its corresponding figure 2. For better readability, these angle dependencies are omitted from the following equations where appropriate

$$\beta(\theta_i, \Phi_i, \theta_r, \Phi_r, \lambda) = \frac{L_r(\theta_i, \Phi_i, \theta_r, \Phi_r, \lambda)}{L_r^{PRD}(\theta_i, \Phi_i, \theta_r, \Phi_r, \lambda)}. \qquad (2)$$

Since the PRD exists only as a theoretical concept and cannot be materialized, the realization of an absolute measurement of the SRF is carried out by measuring the apparatus itself. The derivation for a radiator-based approach, as applied with some history [14] in PTB's goniometric measurements is outlined in [7, 15].

Basic requisites for this approach are that the radiance of the illuminating radiation source $L_i(\lambda)$ must be constant over the entire beam cross-section and for all directions and that the aperture angles of the irradiation and detection paths must be small in order to account for the differential character of the measurand. These conditions are met by the applied sphere radiator at least for commonly used diffuse reflectance standards measured in standard geometries outside the specular direction. The apparatus has a full irradiation aperture angle

of $3°$ and a full detection aperture angle of $0.64°$. Therefore, $L_r^{PRD}(\lambda)$ in equation (2) can be written as:

$$L_r^{PRD}(\lambda) = \frac{\cos\theta_i}{\pi} \cdot \frac{A_Q}{R^2} \cdot L_i(\lambda). \qquad (3)$$

Here A_Q denotes the emitter area, and R the distance between emitter and sample. During measurement the influx radiance $L_i(\lambda)$ as well as the reflected radiance $L_r(\lambda)$ are recorded by measurement of the related photocurrent signals $S_i(\lambda)$ and $S_r(\lambda)$. These are proportional to radiance values and are measured with the same measuring apparatus, with the same optical path and the same measuring electronics. In this ideal case the proportionality factors are equal and cancel out. Accounting for related dark signals $S_{(i,r)d}(\lambda)$, this results in the basic equation for the absolute SRF, which is determined with PTB's gonioreflectometer:

$$\beta(\lambda) = \frac{\pi R^2}{A_Q \cos(\theta_i)} \cdot \frac{S_r(\lambda) - S_{rd}(\lambda)}{S_i(\lambda) - S_{id}(\lambda)}. \qquad (4)$$

2. Measurement uncertainty of the spectral radiance factor

To get an accurate assessment of the measurement uncertainty, a complete as possible list of factors contributing to the uncertainty budget must be identified. Their magnitude is then determined together with the corresponding sensitivity coefficients to result in the final uncertainty value [16]. An insight is given in the following sections, which can be applied to the reference system as well as to the similar ARGon^3 research-gonioreflectometer [8].

2.1. Model for the determination of the uncertainty

The model discussed in the following can be written in symbolic form as:

$$\beta\left(\lambda, R, A_Q, \Delta T, \vec{\Delta}, \vec{\Gamma}, \vec{K}, \vec{C}_{sens}, \vec{S}, T_f, f_{br}, f_{bi}, f_{pol}, f_{fluo}\right)$$

$$= \frac{\pi R^2}{A_Q(\Delta T)\cos\left(\theta_i\left(\vec{\Delta}, \vec{\Gamma}, \vec{K}\right)\right)} \cdot T_f \cdot f_{pol}$$

$$\times \cdot \frac{(c_{sens11} + c_{sens12})S_r \cdot f_{br} \cdot f_{fluo} - (c_{sens21} + c_{sens22})S_{rd}}{f_{bi} \cdot (S_{i1} + S_{i2}) - (c_{sens31}S_{id1} + c_{sens32}S_{id2})}. \qquad (5)$$

The equation (5) arises from the described measuring procedure of the determination of the absolute SRF (equation (4)) and is extended by multipliers of the influencing variables.

The individual dependencies of equation (5) on variables are described in detail below.

A main factor of influence originates from the light source instabilities. For the acquisition of the signals S_i, S_r, the photocurrent is typically averaged n times ($n_{i1} = n_{i2} = 10$, $n_r = 20$) with a time constant of $dt = 1$ s. Thus, short-term statistical fluctuations of the radiance dominate the uncertainty of the measured signals.

Complete data acquisition at one wavelength in one geometry takes about five minutes (t_{meas}), linear drift of the radiance occurring in t_{meas} is accounted for by measuring the signal of the light source before (S_{i1}) and after (S_{i2}) measurement of the reflected radiance and taking the average.

The signals of the light source and of the sample can easily differ by four to five orders of magnitude. Thus, the non-linearity of the detection system (electronics plus detector—here a silicon photodiode in combination with a pico-amperemeter) must be taken into account. Alternatively, a neutral-density filter can be used to attenuate the signal of the light source, so that the then detected signal of the light source and the reflected radiance have the same order of magnitude. Then they can be measured in the same range of the detection electronics.

The wavelength plays an important role either in ranges where the sample's reflectance strongly depends on the wavelength or caused by the strongly structured spectrum of the LED-SR as will be shown in section 3.2.

Geometrical factors have to be accounted for as well. The actual measurement geometry can deviate from the nominal geometry for several reasons: uncertainty in sample positioning and limited reproducibility of sample positioning, non-perfect sample alignment as well as non-planarity of the sample surface.

Temperature-related effects contribute to the uncertainty by the thermal expansion of the precision aperture of the sphere radiator, used to determine the radiating area. This is especially important for the Halogen-SR which, although actively cooled, exhibits aperture temperatures of about $45°C$.

The room temperature and thus the sample under test are actively maintained at $23°C$.

Combining all of the above, the SRF is a function of the following signal- and non-linearity-related input quantities:

$$\vec{S} = \begin{pmatrix} S_r & S_{rd} & S_{i1} & S_{id1} & S_{i2} & S_{id2} \end{pmatrix}. \qquad (6)$$

S_r, S_{rd}: radiance reflected by the sample and corresponding dark signal.

S_{i1}, S_{id1}: radiance of the light source, measured before measurement of the sample, and corresponding dark signal.

S_{i2}, S_{id2}: radiance of the light source, measured after measurement of the sample, and corresponding dark signal.

$$\overrightarrow{C_{sens}} = \begin{pmatrix} c_{sens11} & c_{sens12} \\ c_{sens21} & c_{sens22} \\ c_{sens31} & c_{sens32} \end{pmatrix}. \qquad (7)$$

$c_{sens\,ij}$: correction factors for the non-linearity of the detection system.

λ: wavelength. Includes wavelength precision $\Delta\lambda_p$ and wavelength accuracy with spectral bandwidth $\Delta\lambda_b$ which is corrected by applying the correction factors f_{bx} to the measured signals taking the used bandwidth into account.

f_{bi}, f_{br}: correction factors f_{bx} for the wavelength accuracy with spectral bandwidth $\Delta\lambda_b$ corresponding to the radiance of the radiation source f_{bi} and the measured radiance reflected by the sample f_{br}.

Table 1. Uncertainty contributions for the determination of the spectral radiance factor.

Input quantity X_i	Designation	Value x_i	Distribution	Measurement uncertainty $u(x_i)$	Sensitivity coefficient $c_{i,\mathrm{GUM}}$
S_r	Radiance reflected by the sample	Determined experimentally	Gaussian	Determined experimentally	$\dfrac{(c_{\mathrm{sens11}}+c_{\mathrm{sens12}})f_{\mathrm{br}}f_{\mathrm{fluo}}}{(c_{\mathrm{sens11}}+c_{\mathrm{sens12}})f_{\mathrm{fluo}}f_{\mathrm{br}}S_r-(c_{\mathrm{sens21}}+c_{\mathrm{sens22}})S_{\mathrm{rd}}}$
S_{rd}	Corresponding dark signal	Determined experimentally	Gaussian	Determined experimentally	$\dfrac{-c_{\mathrm{sens21}}-c_{\mathrm{sens22}}}{(c_{\mathrm{sens11}}+c_{\mathrm{sens12}})f_{\mathrm{fluo}}f_{\mathrm{br}}S_r-(c_{\mathrm{sens21}}+c_{\mathrm{sens22}})S_{\mathrm{rd}}}$
S_{i1}	Radiance of the light source, measured before measurement of the sample	Determined experimentally	Gaussian	Determined experimentally	$-\dfrac{f_{\mathrm{bi}}}{f_{\mathrm{bi}}(S_{\mathrm{i1}}+S_{\mathrm{i2}})-(c_{\mathrm{sens31}}S_{\mathrm{id1}}+c_{\mathrm{sens32}}S_{\mathrm{id2}})}$
S_{id1}	Corresponding dark signal	Determined experimentally	Gaussian	Determined experimentally	$\dfrac{c_{\mathrm{sens31}}}{f_{\mathrm{bi}}(S_{\mathrm{i1}}+S_{\mathrm{i2}})-(c_{\mathrm{sens31}}S_{\mathrm{id1}}+c_{\mathrm{sens32}}S_{\mathrm{id2}})}$
S_{i2}	Radiance of the light source, measured after measurement of the sample	Determined experimentally	Gaussian	Determined experimentally	$-\dfrac{f_{\mathrm{bi}}}{f_{\mathrm{bi}}(S_{\mathrm{i1}}+S_{\mathrm{i2}})-(c_{\mathrm{sens31}}S_{\mathrm{id1}}+c_{\mathrm{sens32}}S_{\mathrm{id2}})}$
S_{id2}	Corresponding dark signal	Determined experimentally	Gaussian	Determined experimentally	$\dfrac{c_{\mathrm{sens32}}}{f_{\mathrm{bi}}(S_{\mathrm{i1}}+S_{\mathrm{i2}})-(c_{\mathrm{sens31}}S_{\mathrm{id1}}+c_{\mathrm{sens32}}S_{\mathrm{id2}})}$
$\Delta\lambda_{\mathrm{p}}$	Wavelength precision	Nominal wavelength	Rectangle	$\dfrac{0.1\ \mathrm{nm}}{\sqrt{3}}$	$\dfrac{1}{\beta}\dfrac{\partial\beta}{\partial\lambda}$
f_{bi}	Correction factor for wavelength accuracy caused by spectral bandwidth of the radiation source	Determined experimentally	Triangular	Determined experimentally	$-\dfrac{S_{\mathrm{i1}}+S_{\mathrm{i2}}}{f_{\mathrm{bi}}(S_{\mathrm{i1}}+S_{\mathrm{i2}})-(c_{\mathrm{sens31}}S_{\mathrm{id1}}+c_{\mathrm{sens32}}S_{\mathrm{id2}})}$
f_{br}	Spectral bandwidth correction factor for wavelength accuracy caused by spectral features in the radiance reflected by the sample	Determined experimentally	Triangular	Determined experimentally	$\dfrac{(c_{\mathrm{sens11}}+c_{\mathrm{sens12}})f_{\mathrm{fluo}}S_r}{(c_{\mathrm{sens11}}+c_{\mathrm{sens12}})f_{\mathrm{fluo}}f_{\mathrm{br}}S_r-(c_{\mathrm{sens21}}+c_{\mathrm{sens22}})S_{\mathrm{rd}}}$
c_{sens11}	Correction factors for the non-linearity of the detection system	PTB calibration	Gaussian	PTB calibration	$\dfrac{f_{\mathrm{br}}f_{\mathrm{fluo}}S_r}{(c_{\mathrm{sens11}}+c_{\mathrm{sens12}})f_{\mathrm{fluo}}f_{\mathrm{br}}S_r-(c_{\mathrm{sens21}}+c_{\mathrm{sens22}})S_{\mathrm{rd}}}$
c_{sens21}	Correction factors for the non-linearity of the detection system	PTB calibration	Gaussian	PTB calibration	$-\dfrac{S_{\mathrm{rd}}}{(c_{\mathrm{sens11}}+c_{\mathrm{sens12}})f_{\mathrm{fluo}}f_{\mathrm{br}}S_r-(c_{\mathrm{sens21}}+c_{\mathrm{sens22}})S_{\mathrm{rd}}}$
c_{sens31}	Correction factors for the non-linearity of the detection system	PTB calibration	Gaussian	PTB calibration	$\dfrac{S_{\mathrm{id1}}}{f_{\mathrm{bi}}(S_{\mathrm{i1}}+S_{\mathrm{i2}})-(c_{\mathrm{sens31}}S_{\mathrm{id1}}+c_{\mathrm{sens32}}S_{\mathrm{id2}})}$
c_{sens12}	Correction factors for the non-linearity of the detection system	PTB calibration	Gaussian	PTB calibration	$\dfrac{f_{\mathrm{br}}f_{\mathrm{fluo}}S_r}{(c_{\mathrm{sens11}}+c_{\mathrm{sens12}})f_{\mathrm{fluo}}f_{\mathrm{br}}S_r-(c_{\mathrm{sens21}}+c_{\mathrm{sens22}})S_{\mathrm{rd}}}$

Table 1. Continued

Input quantity X_i	Designation	Value x_i	Distribution	Measurement uncertainty $u(x_i)$	Sensitivity coefficient $c_{i,\text{GUM}}$
c_{sens22}	Correction factors for the non-linearity of the detection system	PTB calibration	Gaussian	PTB calibration	$-\dfrac{S_{\text{rd}}}{(c_{\text{sens11}}+c_{\text{sens12}})f_{\text{fluo}}f_{\text{br}}S_r-(c_{\text{sens21}}+c_{\text{sens22}})S_{\text{rd}}}$
c_{sens32}	Correction factors for the non-linearity of the detection system	PTB calibration	Gaussian	PTB calibration	$\dfrac{S_{\text{id2}}}{f_{\text{bi}}(S_{\text{i1}}+S_{\text{i2}})-(c_{\text{sens31}}S_{\text{id1}}+c_{\text{sens32}}S_{\text{id2}})}$
$\Delta, \Gamma, K_{\text{stat}}$	Deviation caused by the finite precision of setting the angle	0	Rectangle	0.0843 mrad	$\dfrac{1}{\beta}\dfrac{\partial\beta}{\partial\Delta_{\text{stat}}}, \dfrac{1}{\beta}\dfrac{\partial\beta}{\partial\Gamma_{\text{stat}}}, \dfrac{1}{\beta}\dfrac{\partial\beta}{\partial K_{\text{stat}}}$
$\Delta, \Gamma_{\text{just}}$	Deviation caused by misalignment and non-planarity of the sample	0	Rectangle	0.35 mrad	$\dfrac{1}{\beta}\dfrac{\partial\beta}{\partial\Delta_{\text{just}}}, \dfrac{1}{\beta}\dfrac{\partial\beta}{\partial\Gamma_{\text{just}}}$
$\Delta, \Gamma, K_{\text{syst}}$	Deviation caused by misalignment of the instrument	0	Rectangle	0.17 mrad	$\dfrac{1}{\beta}\dfrac{\partial\beta}{\partial\Delta_{\text{syst}}}, \dfrac{1}{\beta}\dfrac{\partial\beta}{\partial\Gamma_{\text{syst}}}, \dfrac{1}{\beta}\dfrac{\partial\beta}{\partial K_{\text{syst}}}$
A_{20}	Irradiating area of the light source	1257.34 mm^2	Gaussian	0.072 mm^2	$1/A_{20}$
ΔT	Temperature difference between ambient temperature and the temperature of the aperture	Typically 25 K	Rectangle	$\dfrac{5\ \text{K}}{\sqrt{3}}$	$\dfrac{2\alpha}{1+\alpha\cdot\Delta T}$
R	Distance between emitter and sample	782.66	Rectangle	$\dfrac{0.25\ \text{mm}}{\sqrt{3}}$	$\dfrac{2}{R}$
T_f	Transmission of a neutral-density filter	PTB calibration	Gaussian	PTB calibration	$1/T_f$
f_{pol}	Correction factor for polarization effects	Determined experimentally	Gaussian	Determined experimentally	$1/f_{\text{pol}}$
f_{fluo}	Correction factor for fluorescence effects of the sample	Determined experimentally	Gaussian	Determined experimentally	$\dfrac{(c_{\text{sens11}}+c_{\text{sens12}})f_{\text{br}}S_r}{(c_{\text{sens11}}+c_{\text{sens12}})f_{\text{fluo}}f_{\text{br}}S_r-(c_{\text{sens21}}+c_{\text{sens22}})S_{\text{rd}}}$

Δ, Γ, K: rotation angle of the sample, tilt angle of the sample, angular position of the rotation stage, all given in apparatus-specific coordinates. These angles must be converted from the measurement geometry (figure 2) [17] to steer the apparatus. Each of the three angle parameters can be described as a sum of several contributions, as shown exemplarily for Δ:

$$\Delta = \Delta_0 + \Delta_{\text{stat}} + \Delta_{\text{syst}} + \Delta_{\text{just}} \qquad (8)$$

where Δ_0 is the nominal angle, Δ_{stat} is the deviation caused by the finite precision of setting the angle, Δ_{syst} is the deviation caused by misalignment of the instrument, and Δ_{just} is the deviation caused by misalignment and non-planarity of the sample.

R: distance between the precision aperture of the light source and the sample surface.

$A_Q (\Delta T)$: irradiating area of the light source, given by

$$A_Q (\Delta T) = A_{20}(1 + \alpha \Delta T)^2 \qquad (9)$$

where A_{20} is the calibrated area of the precision aperture of the light source, determined at $T_{\text{cal}} = 20\ °\text{C}$, α is the thermal expansion coefficient of the aperture material and ΔT is the temperature difference between T_{cal} and the temperature of the aperture.

T_{f}: transmission of a neutral-density filter; this term is only applicable if a filter is used for the measurement of the light source.

f_{pol}: factor to take polarization effects into account. Studies have shown that, depending on the bidirectional geometry and wavelength, the radiation reflected by matte ceramics and other material can be strongly polarized [18]. Even for quasi-Lambertian reflection samples, a large degree of polarization (DOP) can be induced by reflection, also when illuminating with unpolarized light. To study this effect, the polarization of the illumination and detection arm has to be controlled and the SRF has to be determined in various fixed polarization states. Since the emission of the sphere radiator is unpolarized [18], a possible way to achieve this is to measure the complete set of Stokes parameters in reflection and determine their contributions [19]. For this purpose, a special polarization-analyzer unit is placed in the detection path of the apparatus. It consists of a quarter-wave plate which can be rotated in steps of $\Delta \vartheta = \frac{\pi}{8}$ and a fixed linear polarizer ($\varphi = 0$) with respect to the following detection system. Using an eight-step technique [20, 21], the normalized Stokes parameters can be determined for the incident and reflected radiance for each geometry and at each wavelength. These parameters and their respective uncertainties allow in principle to derive a detailed estimation of the influence of the polarization on the uncertainty of the SRF.

The disadvantage of this method is that the measurement time is extended considerably. The determination of the Stokes parameters is necessary at least once to gain an estimate of the magnitude and the influence of polarization effects on the measurement results. To be faster and more effective, for most standard samples and modest geometries like presented here, it is often sufficient to estimate the polarization effects according

to a simplified concept described in section 2.2. For geometries with high influx or efflux angles and or treating special samples, like effect-pigment samples, however, the uncertainty analysis will have to be considered more closely by determining the full Stokes parameters for almost each wavelength position.

f_{fluo}: correction factor for fluorescence effects of the sample. It is known that some standard white materials show fluorescence when being exposed to UV and short wavelength visible radiation [22]. This effect depends on the applied wavelength and is often triggered by short wavelengths. Fluorescence is material specific and the induced error in diffuse reflectance measurements must therefore be considered for the particular sample under test [23].

Specific uncertainty contributions, their magnitudes and how these values were determined are presented and discussed in the next section.

2.2. Uncertainty analysis according to GUM—individual contributions

According to the Guide to the Expression of Uncertainty in Measurement (GUM), all input quantities x_i, their uncertainties $u(x_i)$ and their sensitivity coefficients $c_{i,\text{GUM}}$ have to be determined to result in the total relative uncertainty given for the uncorrelated case by the following equation

$$\frac{u(\beta)}{\beta} = \sqrt{\sum_i \left(c_{i,\text{GUM}} u(x_i) \right)^2}. \qquad (10)$$

The sensitivity coefficients c_i are defined as

$$c_{i,\text{GUM}} = \left| \frac{1}{\beta} \frac{\partial \beta}{\partial x_i} \right|. \qquad (11)$$

All relevant contributions are listed in table 1.

The values of these contributions are determined in different ways.

Some have to be calculated for each data acquisition, e.g. the uncertainties of the measured signals from $\vec{S}$ since they are given by the standard deviation of the average of n signal readings.

Others are determined by externally conducted calibrations performed at specialized divisions of PTB, like the size and uncertainty of the precision aperture A_{20}, the non-linearity coefficients of the detection system $c_{\text{sens}ij}$ and the filter transmission T_{f}. These calibrations have to be performed for each precision aperture, for each combination of current amplifier and detector type and each filter. But as long as those are not changed in the course of the radiance factor measurement, their contributions remain constant or their possible drifts are actively minimized, e.g., the temperature of the precision diaphragm by forced cooling.

Some input uncertainties are estimated by own experiments or given as values supplied by the calibration certificates of the used instruments, as for R, ΔT and partly also λ. The wavelength uncertainty $\Delta \lambda_{\text{p}}$ stemming from the monochromator unit and accounting for the wavelength precision is equal for both types of radiation source presented in the following.

The applied spectral bandwidth of the monochromator can lead to a broadening of sharp spectral features. This wavelength accuracy with spectral bandwidth $\Delta\lambda_b$ can be corrected by a multiplication of the measured signals with the correction factor f_{bx}. It is applicable as correction factor f_{bi} to the radiance of the radiation source and as f_{br} to the measured radiance reflected by the sample. The determination of the correction factor f_{bx} may be performed using different equivalent approaches [24–27]. Here the Taylor-series approach with the assumption of a triangular bandpass function was applied. The correction factor f_{bx} is given then by equation (12) and depends on the used spectral bandwidth $\Delta\lambda$ and the measured signal $\vec{S}$

$$f_{bx}(\vec{S}, \Delta\lambda) = 1 - \frac{1}{12} \cdot \frac{\Delta\lambda^2}{\vec{S}(\lambda)} \cdot \frac{\partial^2 \vec{S}(\lambda)}{\partial\lambda^2}. \tag{12}$$

Since the same apparatus with the same spectral bandwidth of 3 nm is usually used for calibration measurements, the influence of the wavelength accuracy with spectral bandwidth $\Delta\lambda_b$ is affected mainly by the spectrum of the radiator used. Whereas the Halogen-SR provides a slowly varying wavelength dependence of the output signal and therefor only has a small effect of $\Delta\lambda_b$, the LED-SR performance shows a large effect. Its analysis of the wavelength accuracy with spectral bandwidth $\Delta\lambda_b$ and the correction factor f_{bi} is outlined in section 3.2.

The uncertainties related to the instrument angles Δ, Γ, K are determined experimentally. To determine the statistical components Δ, Γ, K_{stat}, a mirror is mounted on the robot, and the deflection of a laser beam is detected when the instrument angles are changed and set repeatedly. E.g., beam deflection experiments with arm-length of 5 m result in an angular uncertainty of

$$u(\Delta_{stat}) = u(\Gamma_{stat}) = u(K_{stat}) = \frac{1}{\sqrt{3}} \frac{0.73 \text{ mm}}{5000 \text{ mm}}$$
$$= 0.0843 \text{ mrad}. \tag{13}$$

The factor $1/\sqrt{3}$ accounts for the rectangular distribution of the input quantity.

The alignment of the sample surface relative to the optical axis is performed using fringe projection. This does not only supply information on the sample alignment, but also on the topography of the sample surface, which might not be perfectly plane. Due to a possible structure and waviness of the surface, different portions of the incident beam will experience different incident and reflection angles, which differ from the nominal angles. The total SRF can be considered to be an integral over these 'sub-geometries', thus the surface topography and the resulting limited angle precision can contribute to the uncertainty, too.

The detector's field of view is given by a circle of 20 mm diameter on the sample surface, elongated by the detection angle of the bidirectional geometry. Therefore, only the surface topography in this area contributes to the uncertainty.

In case of standard geometries and the measurement of reflection standards with a smooth and even surface, the influence of the curvature of the surface is small and can be estimated by the alignment uncertainty. In extreme cases, with special geometries and uneven samples, influence can be significantly larger and must be estimated differently.

Unlike special topography of the surface, a global wedge angle of the sample surface for one direction can be compensated by the alignment process. The corresponding value representing the uncertainty contribution of the alignment precision can be sample dependent. For the ceramic samples presented in this publication, this contribution for the alignment precision is estimated to be $u(\Delta_{just}) = u(\Gamma_{just}) = 0.35$ mrad.
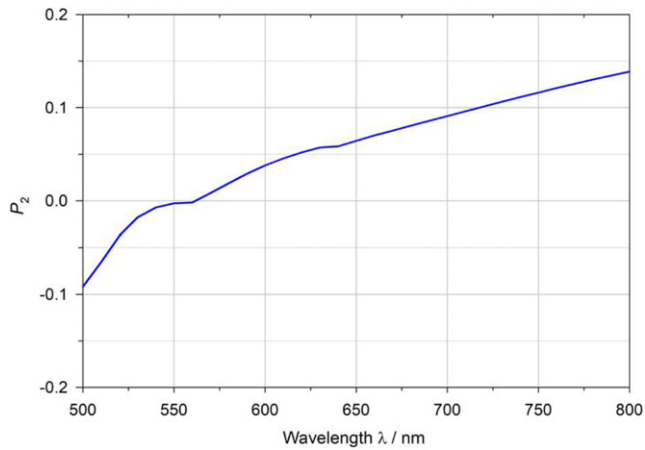
Another point to account for is the finite irradiation aperture angle of the sphere radiator, which amounts to a full angle of $3°$. Depending on the geometry considered, the partial beams are not exactly equal in geometry because of beam divergence and because the measurement area in most cases forms an ellipse on the sample. This influence increases for high incident angles. For standard geometries like the geometry presented here, this effect is negligibly small.

The estimation of polarization effects which can be found in reflection measurements can be treated according to [19, 28, 29]. In principle, all polarization parameters can be determined by experiment, however these measurements are often time consuming. When the influence of polarization is small, as for the standard geometries discussed here, procedures can be given to correct deviations in the resulting SRF, if polarization is not explicitly taken into account in the measurement. For all typical white standards, linear polarization aligned to the main axes of the scattering experiment, described by the Stokes parameter M_0, is by far the dominating quantity [18]. The procedures described in [28, 29] use this fact and equation (14) can be derived from equations (A3) and (A5) in [29], which describe the influence of polarization in irradiation (P_1) and detection (P_2) on the SRF-result. Taking into account that the irradiation with the sphere radiators is unpolarized ($P_1 = 0$), only the detection path factor P_2 has to be dealt with. In equation (14), β_{rr} is the unpolarized SRF to be determined when β_m is the measured SRF, taken without polarization analysis. The relative difference only depends on the polarization induced by reflection on the sample and on the polarization sensitivity of the detection path. The deviation of the SRF and thus the polarizations effect scales linearly with P_2, which is the product of the DOP of the detection path and the Stokes parameter M_0 for linear s- or p-polarizations.

$$\Delta\beta = \frac{\beta_m - \beta_{rr}}{\beta_{rr}} = -P_2 \cdot M_0 = -\frac{S_s - S_p}{S_s + S_p} \cdot M_0. \tag{14}$$

For commonly used white standards linear polarization with respect to the main axes is the dominating quantity and a full polarization analysis can be avoided by making use of equation (14). For this purpose, the polarization sensitivity P_2 in the detection path of the apparatus and the polarizing property M_0 of the sample class in terms of geometry and wavelength must be known. In the set-up presented here, P_2 is dominated by the gratings of the analyzing double-monochromator (figure 1). Additionally, the detection
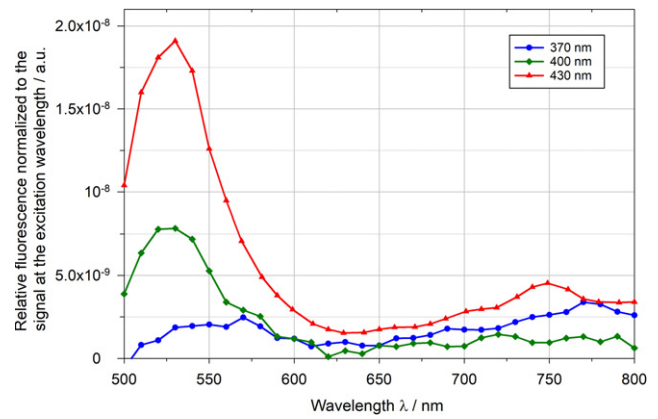
Figure 3. Polarization sensitivity P_2 in the detection path as function of wavelength.

Figure 4. Relative fluorescence of a white matte ceramic normalized to excitation wavelength of 370 nm, 400 nm, and 430 nm.

path is performing a physical frame rotation by its mirrors which mixes occurring polarization components. The resulting wavelength-dependent sensitivity can be measured by determination of the maximum polarization modulation with a linear polarizer when illuminating with unpolarized radiation. P_2 for the visible spectral range is depicted in figure 3.

Around 560 nm P_2 passes through zero, when sensitivity for parallel and perpendicular components are equal. For the white, red, and the blue samples at 700 nm with $\beta_i = (0.925, 0.807, 0.124)$ and $M_{0,i} = (-0.015, -0.0188, -0.113)$ corrections according equation (14) of $\Delta\beta_i = (-1.6 \times 10^{-3}, -2.4 \times 10^{-3}, -4.7 \times 10^{-4})$ result. As experimental and calculated values in the mean do agree by about $|\Delta\beta_i| = 5 \times 10^{-4}$, the latter value can be regarded as an additional uncertainty introduced, when the simplified polarization treatment is applied. Observed corrections are of the order of the total uncertainty and therefore cannot be ignored at the presented uncertainty level.

The matte ceramic tiles presented here, particularly the white sample, exhibit a small amount of fluorescence emitted in bands from (500–600) nm and (700–900) nm when irradiated with short wavelength visible to near-UV radiation. To account for this fluorescence in the uncertainty calculation a fluorescence correction factor can be determined. To obtain an estimate of the fluorescence amount excited by the sample at a given wavelength and intensity, the LED-SR is used. Being applied as broadband emitter, single wavelengths can be selected by inserting interference filters in 10 nm steps. The fluorescence of the sample at these excitation wavelengths is recorded using a sensitivity-corrected CCD sensor. A sample-specific fluorescence curve is determined as a function of excitation wavelength and intensity. This relative fluorescence normalized to the excitation wavelength is shown exemplarily for the white matte ceramic sample with excitation wavelengths of 370 nm, 400 nm, and 430 nm (figure 4). The fluorescence effect increases with wavelength.

To obtain a corresponding photocurrent value, the normalized fluorescence must be related to the respective irradiation at the excitation wavelength. To account for the fluorescence of

the sample in SRF measurements two aspects have to be considered. First, the fluorescence portion in the spectral range in which fluorescence was detected must be subtracted from the measured diffuse reflectance of the sample, because the determined sample-specific fluorescence is measured in addition to the 'true' diffuse reflectance of the sample. Second, the determined sample-specific fluorescence as a function of the respective excitation wavelength corresponds exactly to the signal that excites the fluorescence and is therefore absent in the diffuse reflection of the sample at the specific excitation wavelength. Therefore, the integrated fluorescence at each excitation wavelength must be added to the corresponding measurement signal of the excitation wavelength. The uncertainty contribution of the fluorescence correction was estimated from the change in SRF when the correction was applied compared to the uncorrected values of SRF. The determined uncertainty contribution of the white ceramic sample fluorescence is in the range of 4.4×10^{-4} in the excitation spectral range from 360 nm to 430 nm and max. 3×10^{-5} in the fluorescence spectral range above 500 nm. The fluorescence for the low reflecting red and blue sample are significantly smaller and can be neglected.

3. Results and discussion

To study the magnitude of the different uncertainty contributions and elucidate major contributions, the SRF has been determined for some matte ceramic samples. A photo of a typical purchasable set is shown in figure 5. The ceramic tiles have a circular shape with a diameter of 50 mm. In this paper, for sake of simplicity we present results for the white, red and the blue ceramic.

### 3.1. Ceramic samples, VIS spectral range

The SRF for the visible spectral range, measured with the Halogen-SR, is shown in figure 6. These results have been obtained with one repetition and 20-fold readings per measurement point in the geometry $\theta_i = 45°$, $\phi_i = 0°$, $\theta_r = 0°$, $\phi_r = 0°$ abbreviated as 45°/0° [30]. All following considerations refer to a coverage factor of $k = 1$.

Figure 5. Set of matte ceramic samples. The white (left), red (third from right) and the blue (right) samples are used to obtain the results presented in this paper.
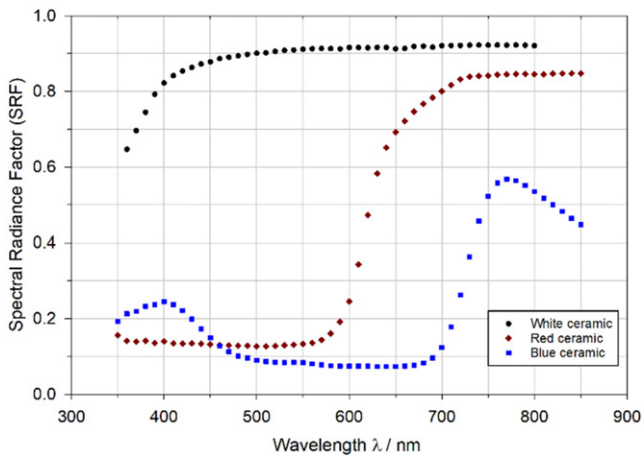

Figure 6. Absolute SRF in the visible spectral range of a white, red and blue ceramic sample determined using the Halogen-SR in 45°/0° geometry and detected with a silicon photodiode.
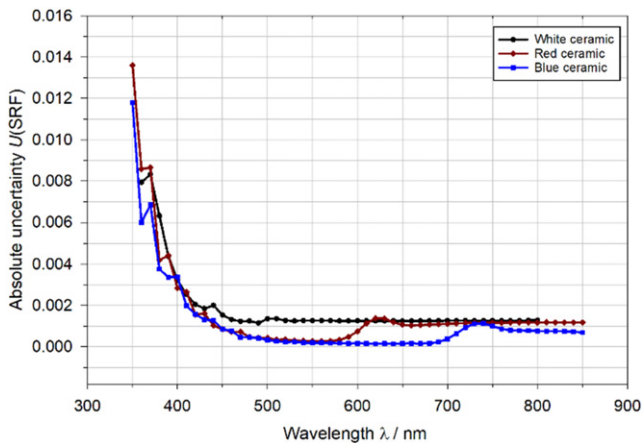

Figure 7. Total absolute measurement uncertainty ($k = 1$) of the absolute SRF for a white, red and blue ceramic sample measured with the Halogen-SR.

For visualization the total absolute measurement uncertainty is shown separately in figure 7.

It can be seen that for most of the visible spectral range, the combined measurement uncertainty is below 1.5×10^{-3}, but it increases steeply below 450 nm. This increase is caused
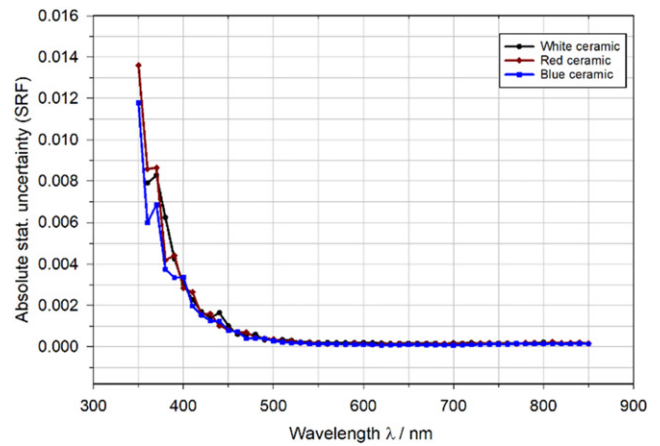
Figure 8. Statistical uncertainty. Below 450 nm, the steep increase is caused by the rapid decrease of the radiance of the Halogen-SR.
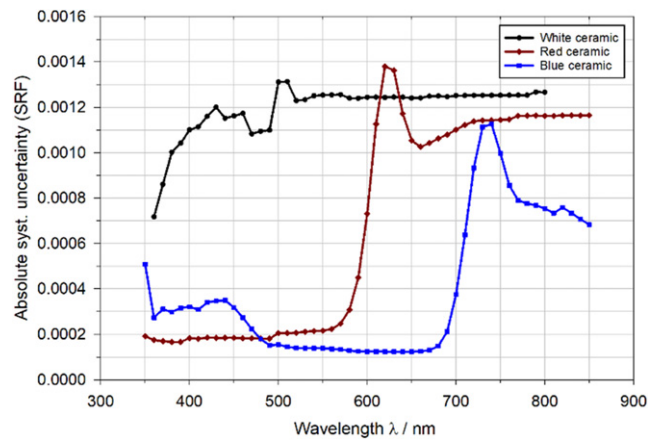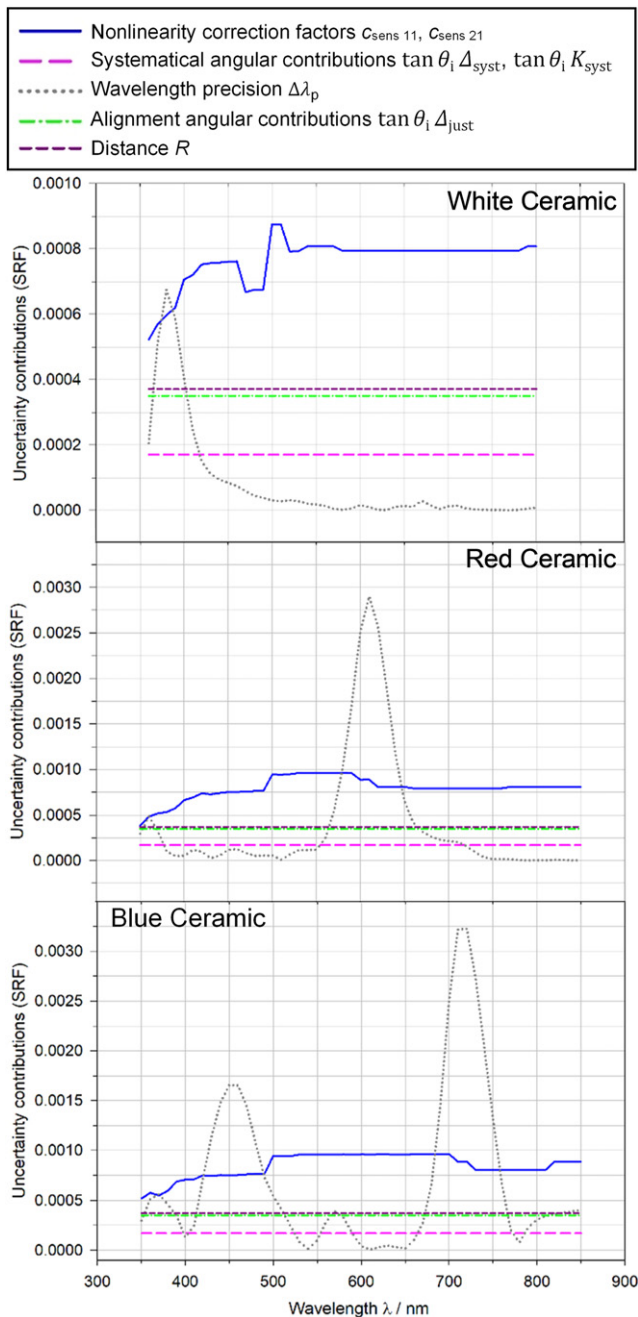

Figure 9. Systematic uncertainty contributions.

by statistical contributions obtained in the 20-fold readings per measurement point, especially by $u(S_r)$, as shown in figure 8. As the radiance of the Halogen-SR decreases below 450 nm, the reflected radiance gets very low, leading to higher statistical uncertainty, which dominates the combined uncertainty then.

Above 450 nm, the combined uncertainty is dominated by systematic contributions, which is shown in figure 9. The largest relative systematic contributions apart from sample properties such as f_{pol} and f_{fluo} are shown in figure 10.

The non-linearity correction coefficient c_{sens11} and c_{sens12} show a wavelength dependency, which is mainly dominated by the magnitude of the available signal. This varies as a combined result of lamp emission, radiator throughput, and optical detection path throughput (mirrors, polarizer components, gratings) and detector efficiency across the observed spectral range. The wavelength dependent change of these parameters and therefore of the resulting signal requires some switching of the currently used pico-amperemeter with related uncertainties.

Other wavelength dependent contributions are resulting from the different spectral shapes of the samples (white or colored). These contributions are highest where the slope in the reflection characteristic is steepest.

Figure 10. The five largest relative systematic uncertainty contributions for the white sample (top panel), red sample (center panel), blue sample (bottom panel).

The wavelength-independent uncertainty of the geometrical distance R also contributes strongly. Other important uncertainty contributions stem from the alignment angles Δ_{just}, Δ_{syst} and K_{syst}. All other contributions are below 10^{-4} and are therefore not shown explicitly in the graphs.

The total absolute uncertainty as well as the absolute systematic and statistical uncertainty contribution for the white, red and blue ceramic measurement presented here as well as for a standard white sintered polytetrafluoroethylene (PTFE) sample can be found in the supporting material (https://stacks.iop.org/MET/59/025004/mmedia).
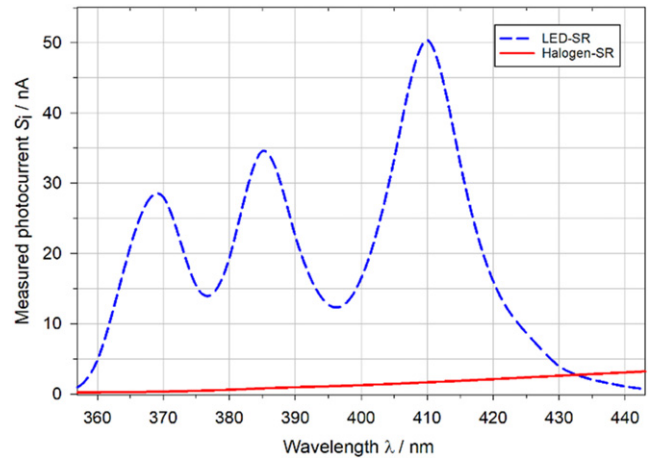
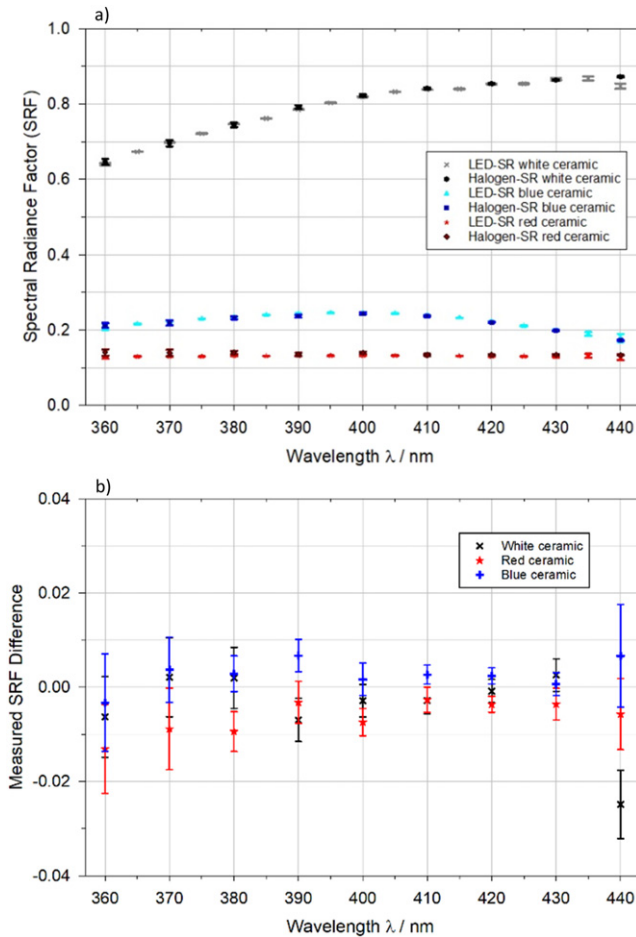**Figure 11.** Measured photocurrent of the Halogen-SR (red line) and the LED-SR (blue dashed).

3.2. Ceramic samples, UV/VIS transition spectral range

As described in the section 3.1 the achievable measurement uncertainty for wavelengths towards UVA is dominated by statistical effects according to the decreasing output power of the Halogen-SR. This is shown by the red curve in figure 11. The newly designed LED-SR produces a significantly higher irradiance below 430 nm, resulting in improved signal quality and stability in its design spectral range [31, 32], as indicated by the measured photocurrent.

For comparison of the radiators' performance, the absolute SRF of the white, red and blue ceramic in the geometry 45°/0° was determined for the spectral range from 360 nm to 440 nm using both sources (figure 12). For consistency these results have been also obtained with a single repetition and 20-fold readings per measurement point. The determined values for all three samples and both radiation sources agree with each other. For each sample measured with both radiators the resulting statistical uncertainties are given in figure 13.

In case of the white ceramic measured with the Halogen-SR, statistical uncertainties begin to dominate the total uncertainty below 430 nm and result in a rise towards shorter wavelengths. In calibrations this can be compensated by a higher number of repetitions or by switching to a more sensitive detector type, possibly causing other drawbacks. For example, the detector can be changed from the used silicon photodiode to the yellow enhanced channel photomultiplier to be able to measure even more sensitively in this spectral range. However, this cannot be changed during the measurement, which leads to an interruption and is not practical in long calibrations especially if the long VIS spectral range is also considered.
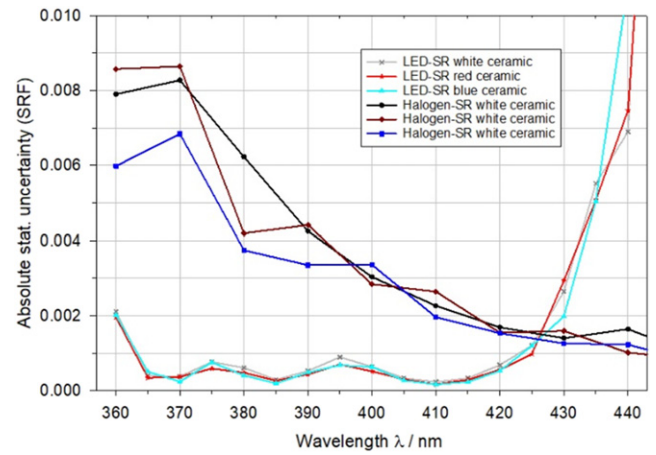
The statistical uncertainty resulting from the LED-SR stays constant and only rises around 365 nm when the available power decreases. Therefore, the statistical contributions are very small for this source in its design spectral range. This is underlined by the uncertainty contributions for the low-reflective blue and red samples, which turn out to be only moderately higher than for the white standard. The break-even point on the long wavelength side is around 425 nm for the
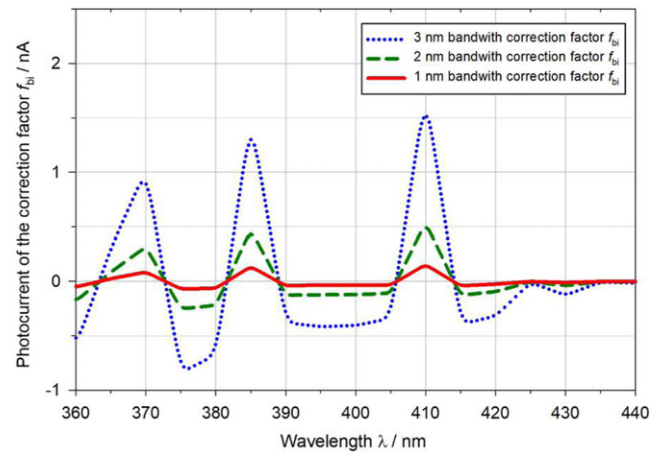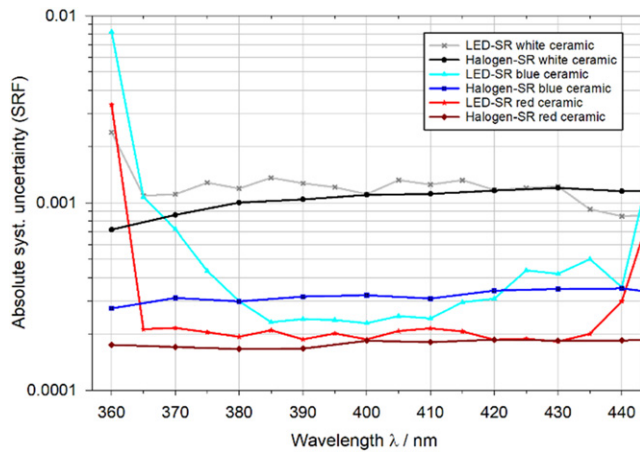
Figure 13. Statistical uncertainty of the absolute SRF for a white, red and blue ceramic sample measured with Halogen-SR and LED-SR in 45°/0° geometry.

Figure 12. (a) Absolute 45°/0°-SRF of a white, red and blue ceramic sample measured with Halogen-SR and LED-SR detected with a silicon photodiode (error bars plotted for $k = 1$). (b) The corresponding measured SRF difference $\beta_{\text{LED-SR}} - \beta_{\text{Halogen-SR}}$ obtained by using both radiation sources and the corresponding uncertainty resulting from error propagation.

Figure 14. Calculated photocurrent of the correction factor f_{bi} of the LED-SR signal S_{i} for different spectral bandwidths $\Delta \lambda$ of 3 nm, 2 nm and 1 nm.

measurements on the three ceramic samples. The statistical uncertainties of the LED-SR between 370 nm and 420 nm are about one order of magnitude smaller than for the Halogen-SR.

Whereas statistical contributions are greatly reduced by the application of the LED-SR (figure 13) due to its higher available radiance and very good temporal stability, a photocurrent change of only 1.7×10^{-5} nA h^{-1} [12, 31, 32] is observed, the wavelength dependent emission of this source measured with the finite bandwidth of the monochromator has to be taken into account in the uncertainty consideration. Some bandwidth-related wavelength uncertainty is introduced by the LED-SR due to its structured spectrum with rising and falling edges, stemming from the individual form of the three LED-peaks (figure 11). For measurements with the Halogen-SR with its smoothly rising spectrum, the bandwidth influence on the wavelength accuracy has a small effect. In case of the LED-SR the resulting wavelength uncertainty component as a function of the bandwidth of the monochromator influences the achievable total uncertainty to a higher extent. As mentioned in section 2, the correction of the wavelength accuracy with spectral bandwidth $\Delta \lambda_{\text{b}}$ is performed by using the

Taylor series approach with the assumption of a triangular bandpass function. The resulting bandwidth-related photocurrent of the correction factor f_{bi} of the LED-SR signal S_{i} for different spectral bandwidths $\Delta \lambda$ are shown in figure 14.

It is obvious that the correction factor f_{bi} increases with larger bandwidth of the monochromator. The extreme points of the correction correlate with the second derivative, more precisely the curvature of the SRF. The use of a small bandwidth would be beneficial for a smaller correction factor. But since a smaller bandwidth is associated with a reduction in throughput, this also leads to a decrease in the measured photocurrent and to a corresponding increase of its standard deviation. In an uncertainty optimized approach the optimal combination of measurement time (repetitions) and bandwidth can be determined, but often the bandwidth is predefined and no optimization can be performed. The accuracy of the correction algorithm, meaning how close the bandwidth corrected spectrum is to the 'true' spectrum was considered using the proposed CIE-methods in [27] and evaluated by simulating the convolution influence on the SRF, since this is the measure
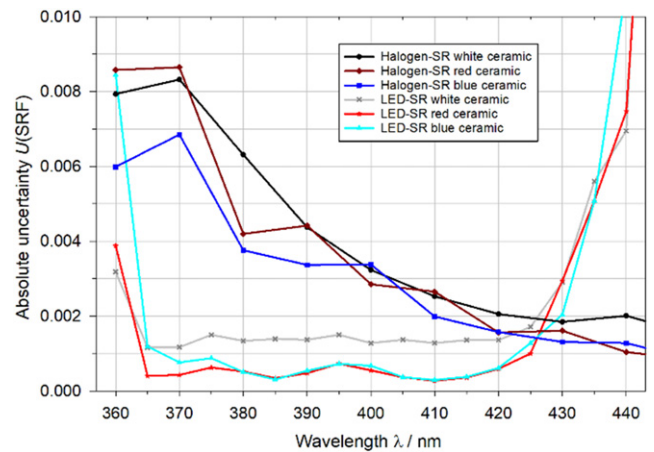
Figure 15. Absolute systematic uncertainty of the SRF for a white, red and blue ceramic sample measured with Halogen-SR and LED-SR in 45°/0° geometry. For a better visualization, a logarithmic representation is used.

Figure 16. Total measurement uncertainty ($k = 1$) of the SRF for a white, red and blue ceramic sample measured with Halogen-SR and LED-SR in 45°/0° geometry.

of quality. The uncertainty contribution of the used bandwidth correction on the SRF measurement can be estimated by the relative deviation determined between the deconvoluted and measured spectrum. While many of the systematical contributions can be assumed to be the same for both radiation sources, the wavelength accuracy with spectral bandwidth $\Delta\lambda_b$ of the LED-SR and its correction f_{bx} is of special importance. For a bandwidth of 3 nm the total systematic uncertainties are plotted for both radiators in figure 15.

From the plot it can be seen that even for a measurement with 3 nm bandwidth including its correction and uncertainty contribution the systematical uncertainties in the spectral range between 370 nm to 420 nm for the LED-SR are only slightly higher than for the Halogen-SR. The wavelength influence on the systematical uncertainty is inversely proportional to the sample's reflectivity and increases below 370 nm. But even this influence is compensated in the combined measurement uncertainty consideration by the resulting smaller statistical effects of the LED-SR. The total measurement uncertainty for the examined samples is shown in figure 16.

Independent of the sample type, the determined combined measurement uncertainty is considerably smaller when applying the LED-SR in the spectral range from 360 nm to 420 nm, compared with a use of the Halogen-SR. The break-even point is around 425 nm, slightly varying with sample color. Sample-specific influences such as the considered fluorescence of the white ceramic contribute greatly to the total uncertainty of both radiators. But despite a conspicuous increase of the total uncertainty below 365 nm measured with the LED-SR, which is especially noticeable with the low-reflecting red and blue samples and stemming from the drop-down of LED-SR output, the determined measurement uncertainty can be still reduced with the LED-SR compared to the Halogen-SR.

For an infinite number of measurements, the total uncertainty approximates the systematic uncertainty. In this case the Halogen-SR would be preferable because of its predominantly smaller systematic uncertainty. But considering a realistic number of measurements, the use of the LED-SR in its designed spectral range would be beneficial and time sav-

ing. The reason is the statistical uncertainty, which is mainly dominated by the standard deviation and reduces only with the root of measurement repetitions and therefore determines measurement time.

The comparative number of measurement repetitions N required for the Halogen-SR to achieve the same total uncertainty as using the LED-SR as figure of merit can be calculated by equation (15). This estimation can be performed by using the measurement data and its uncertainty analysis shown in this paper since they represent one usual measurement repetition with 20-fold readings per measurement point. Here u_{stat} denotes the statistical, u_{sys} the systematical uncertainty contributions and U the total measurement uncertainty respectively for the LED- or Halogen-SR.

$$N = \frac{u_{\text{stat Halogen−SR}}^2}{U_{\text{LED−SR}}^2 - u_{\text{sys Halogen−SR}}^2}. \tag{15}$$

Thus, the number of repetitions N required by the Halogen-SR to achieve the same combined standard uncertainty obtained with the LED-SR with only one repetition can be sized. E.g., for the previously shown white, red and blue ceramic samples at 390 nm 22, 98 and 58 measurement repetitions with the Halogen-SR are needed to achieve the same measurement uncertainty as with the LED-SR. This improvement and effectivity even increase up to 370 nm.

Therefore, the application of LED-SR for the measurement of the absolute SRF leads to a significant improvement with respect to the achievable measurement uncertainty for the UV/VIS transition spectral range. With the use of the LED-SR, an approach to minimize measurement uncertainties in combination with a reduction of the measurement time was achieved.

4. Conclusion

We present a detailed uncertainty analysis for goniometric absolute SRF measurements. The influence and contribution of the individual identified uncertainty sources on the com-

bined uncertainty was explained theoretically. As a specific example we described the determination of the absolute SRF measurement in a 45°/0° geometry for three ceramic samples with different reflection properties. Some uncertainties such as polarization effects and fluorescence depend on the specific properties of the sample and must be taken into account when analyzing the measurement uncertainty. A possibility to consider these influences and to include them in the uncertainty calculation was shown.

The combined measurement uncertainty in the visible spectral range between 450 nm to 850 nm is below 0.16% and is mostly affected by systematic contributions like the nonlinearity correction coefficients for the detection electronics. Towards shorter wavelengths, statistical effects due to the decreasing power of the halogen-based radiation source overlay these systematic effects and represent the largest uncertainty influence. To minimize these uncertainty contributions a specially designed LED based sphere radiation source for UV/VIS transition measurements was used. As a result, the measurement uncertainty in the range between 360 nm and 425 nm could be significantly reduced depending on the sample and wavelength (figure 16). For example, at 390 nm the measurement uncertainty for the white, red and blue ceramic sample could be reduced by a factor of 3, 9 and 6, respectively.

In the future work this first approach of the LED-SR should be extended to deeper UV spectral ranges. In addition, the LED-SR has the potential to be operated in a pulsed mode in combination with a lock-in amplifier [31], which provides an even better signal-to-noise ratio and reduced sample irradiation.

Acknowledgments

Conflict of interest

The authors declare no conflicts of interest.

ORCID iDs

Irina Santourian ⓘ https://orcid.org/0000-0001-8718-8947
Alfred Schirmacher ⓘ https://orcid.org/0000-0002-2228-7853

References

[1] ASTM E12 Committee 2019 ASTM E2387-19 Practice for goniometric optical scatter measurements *Book of Standards Volume: 06.01* (ASTM International) https://doi.org/10.1520/E2387-19

[2] Deutsche Institut für Normung e. V. (DIN) 1978 DIN 5036-1: Strahlungsphysikalische und lichttechnische Eigenschaften von Materialien (Beuth Verlag GmbH) https://doi.org/10.31030/1114183

[3] Commission International d'Eclairage (CIE) 1977 Radiometric and photometric characteristics of materials and their measurement *CIE Publication No. 38 (TC-2.3)* CIE Committee

[4] See e.g. the scientific programs xDReflect (https://xdreflect.eu), BiRD (https://birdproject.eu/u/references/bibliography on white standard) and BxDiff (https://bxdiff.cmi.cz/)

[5] Georgiev G and Butler J 2008 BRDF study of gray-scale spectralon *Proc. SPIE-Int. Soc. Opt. Eng.* 7081

[6] Höpe A, Hauer K, Bergner P and Ziegler T 2014 BRDF measurements at 254 nm for the LISA Pathfinder satellite mission *Proc. of New Developments and Applications in Optical Radiometry (NEWRAD)*

[7] Hünerhoff D, Grusemann U and Höpe A 2006 New robot-based gonioreflectometer for measuring spectral diffuse reflection *Metrologia* **43** S11–6

[8] Höpe A, Atamas T, Hünerhoff D, Teichert S and Hauer K-O 2012 ARGon3: '3D appearance robot-based gonioreflectometer' at PTB *Rev. Sci. Instrum.* **83** 045102

[9] Hauer K-O and Höpe A 2008 High-grade uniform light source for radiometric and photometric applications *MAPAN* **24** 175–82

[10] Santourian I, Teichert S, Hauer K-O and Schirmacher A 2019 Investigation of the suitability of high-power LEDs for the use as radiation source for PTB's gonioreflectometer *Lux junior 2019: 14. Internationales Forum für den lichttechnischen Nachwuchs* (Dörnfeld/Ilm, 6–8 September 2019) pp 43–50

[11] Santourian I, Teichert S, Hauer K-O, Quast T and Schirmacher A 2021 Further development of an LED-based radiation source for goniometric spectral radiance factor measurements *Lux junior 2021: 15. Internationales Forum für den lichttechnischen Nachwuchs* (Online - Technische Universität Ilmenau, 4–6 Juni 2021) pp 255–63

[12] Santourian I, Quast T, Teichert S, Hauer K-O and Schirmacher A 2022 Novel LED-based radiation source and its application in diffuse reflectometry and polarization measurements *J. Phys.: Conf. Ser.* **2149** 012010

[13] Zwinkels J C, Germer T A and Tsai B K 2014 Experimental methods in the physical sciences *Spectrophotometry: Accurate Measurement of Optical Properties of Materials* Experimental Methods in the Physical Science vol 46 (Amsterdam: Elsevier)

[14] Erb W 1987 High-accuracy gonioreflectance spectrometry at the PTB *Advances in Standards and Methodology in Spectrophotometry* vol 2 (Amsterdam: Elsevier) pp 87–98

[15] Strohtkämper C *et al* 2017 Multilateral spectral radiance factor scale comparison *Appl. Opt.* **56** 1996–2006

[16] International Organization for Standardization (ISO) 1993 *Guide to the Expression of Uncertainty in Measurement (GUM)* 1st edn (International Organisation for Standardization) corrected, reprinted and supplemented several times, latest reissue 2021

[17] Mescheder L 2013 Differentialgeometrische Betrachtung eines Roboterbasierten Gonioreflektometers *Bachelor Thesis* Technische Universität Braunschweig, Braunschweig

[18] Quast T, Schirmacher A, Hauer K-O and Koo A 2018 Polarization properties and microfacet-based modelling of white, grey and coloured matte diffuse reflection standards *J. Phys.: Conf. Ser.* **972** 012024

[19] Quast T and Schirmacher A 2020 BRDF and polarisation—pitfalls and how to avoid them *Online Tutorial: 5th CIE Expert Symp. on Colour and Visual Appearance*

[20] Zdenek S 1956 Recent developments in the study of the polarization of sky light *Advances in Geophysics* vol 3 (Amsterdam: Elsevier) pp 43–104

[21] Fröhling R and Andrä H J 1983 Observation of Na I inner shell-excited quartet terms *Phys. Lett.* A **97** 375–6

[22] Shitomi H and Saito I 2006 Photoluminescence from white reference materials for spectral diffuse reflectance measurements upon exposure to radiation shorter than 400 nm *Metrologia* **43** 36–40

[23] Pons A and Campos J 2004 Spectrophotometric Error in colour coordinates Introduced by Fluorescence of white calibration tile *Color Res. Appl.* **29** 11–4

[24] Woolliams E R, Baribeau R, Bialek A and Cox M G 2011 Spectrometer bandwidth correction for generalized bandpass functions *Metrologia* **48** 164–72

[25] Gardner J L 2006 Bandwidth correction for LED chromaticity *Color Res. Appl.* **31** 374–80

[26] Schinke C, Pollex H, Hinken D, Wolf M, Bothe K, Kröger I, Nevas S and Winter S 2020 Calibrating spectrometers for measurements of the spectral irradiance caused by solar radiation *Metrologia* **57** 065027

[27] Commission International d'Eclairage (CIE) 2014 Effect of instrumental bandpass function and measurement interval on spectral quantities *CIE Publication No. 214 (TC 2-60)* CIE Committee

[28] Clarke F J J, Garforth F A and Parry D J 1983 Goniophotometric and polarization properties of white reflection standard materials *Light. Res. Technol.* **15** 133–49

[29] Calderón A, Ferrero A and Campos J 2020 Accounting for polarization-related effects in the measurement of the bidirectional reflectance distribution function *Metrologia* **57** 045003

[30] Deutsche Institut für Normung e. V. (DIN) 1979–2021 *DIN 5033: Farbmessung - Teil_1 bis 10* (Beuth Verlag GmbH)

[31] Santourian I *PhD Thesis* in preparation, expected to be published 2022

[32] Santourian I, Teichert S, Schirmacher A, Quast T and Hauer K-O 2021 Construction and characterization of a high-power UV-LED module as radiation source for goniometric spectral radiance factor measurements *ICULTA—The Int. Conf. on UV LED Technologies & Applications*